Journal Name

ARTICLE

Hierarchical NiO-In_2O_3 Microflower (3D)/ Nanorod (1D) Hetero-Architecture as a High Performance Supercapacitor Electrode with Excellent Cyclic Stability

Received 00th January 20xx,
Accepted 00th January 20xx

DOI: 10.1039/x0xx00000x

www.rsc.org/

N. Padmanathan[a], Han Shao[a,b], David McNulty[b], Colm O'Dwyer[a,b] and Kafil. M. Razeeb[a,*]

Three-dimensional (3D) hybrid nanostructured electrodes based on one-dimensional (1D) nanorod arrays have recently attracted great attention owing to their synergistic effect of three-dimensional nanostructures and application in energy storage and conversion devices. Here, we designed a heterostructured supercapacitor electrode from a combination of NiO and In_2O_3 with a hierarchical hybrid microstructure on nickel foam (NF). Simultaneous heterogeneous growth of 1D nanorod-supported 3D microflower structures on nickel foam enhanced the pseudocapacitance performance due to the synergistic contribution from hierarchical hybrid nanostructure. The heterostructured electrode exhibits a high specific capacitance of 1096.8 F g^{-1} at 5 A g^{-1} and remains as high as 407.1 F g^{-1} at 30 A g^{-1}, which are significant than their individual oxides. The composite electrode shows an excellent rate performance as a sandwich type symmetric device, offering a high specific energy density of 21.1 Wh kg^{-1} at a high power density of 1500 W kg^{-1}. The device shows a long term cyclic stability with 79% capacitance retention after 50,000 cycles, which is remarkable for an oxide based capacitor. These results suggest that NiO-In_2O_3 with hybrid micro/nano architecture could be a promising electrode for next generation high performance supercapacitors.

Keywords: Advanced functional materials, Energy storage, Heterostructure electrodes, Supercapacitor, Pseudocapacitance

Introduction

Sustainable and renewable green energy sources, in conjunction with conventional energy storage systems, such as rechargeable batteries and supercapacitors (SCs), are one of the key solutions to alleviate the critical problems of the escalating energy crisis and environmental issues derived from consumption of fossil fuels.[1-5] Unique features of supercapacitors such as high power density, fast charging time, safe, long lifespan and excellent reliability enabled them to be potentially used as power sources in various technological devices.[1,5] However, the energy density of state of the art supercapacitors is still not comparable to the batteries, mainly due to inadequate performance of the electrode materials. Therefore, supercapacitors have not seen the rate of improvement found for batteries until recent years because of lack of understanding of the origin of their excellent specific capacitances, and the difficulties in fabrication of novel electrode materials with tunable compositions and microstructures.[6] In order to improve further the performance of supercapacitors, it is highly desirable to fabricate materials with not only a high electrochemical activity, but also a stable hierarchical structure with excellent ability for electron transportation and negligible ion diffusion time.[1-6]

When compared to traditional carbon based materials pseudocapacitive materials can obviously enhance the specific capacitance and energy density of the supercapacitors via interfacial faradaic reactions to store energy.[1,7] Thereby, pseudocapacitive materials including RuO_2,[8] MnO_2,[9] NiO,[10-13] Co_3O_4[11,14] and their composite systems possess high pseudocapacitance but suffer from low rate capability and reversibility due to their dependence on faradic redox reactions to store charge and the low conductivity of the oxide.[15] Numerous studies have shown that the charge-storage properties of pseudocapacitors depend not only on the nature of electrode materials but also greatly on the design of these electrodes.[16] Therefore, in recent years, the extensive advancements in supercapacitor performance have been due to the optimization of microstructure of the electrode materials in particular, nanocrystalline hetero-structures exemplify an interesting approach in developing nanoscale building blocks for fabricating highly efficient electrodes.[17] Among those, 3D/1D-hierarchical micro/nano heterostructure

[a] Nano-Interconnection, Tyndall National Institute, University College Cork, Dyke Parade, Lee Maltings, Cork, Ireland.
[b] Department of Chemistry, University College Cork, Cork, Ireland
*Corresponding Author: Dr. Kafil M. Razeeb (kafil.mahmood@tyndall.ie)
† Footnotes relating to the title and/or authors should appear here.
Electronic Supplementary Information (ESI) available: [details of any supplementary information available should be included here]. See DOI: 10.1039/x0xx00000x

are attractive and can improve ion/electron transport at the electrode/ electrolyte interface by utilizing the high surface area of the nanocrystalline structure to perform the faradic reaction and highly conductive microstructure backbone to provide low resistance path for the electron transport.[18-23]

Since the invention of the pseudocapacitor, NiO has been comprehensively investigated as an electrode for pseudocapacitors due to its abundance, low cost and high theoretical capacitance of 2573 F g^{-1},[24-27] whereas, a capacitance of 2018 F g^{-1} has been achieved so far for the NiO based nanowires.[10] But like other metal oxide electrodes, it suffers from capacity decay with cycling resulting from the collapse of nanostructures, low intrinsic conductivity and large volume change during faradaic reaction.[28-30] To address these problems, one approach is to design hybrid hetero-structures with different materials either carbon or non-carbon supports which can improve the electrode performance due to synergistic effects between two components.[31] Generally, carbon supports lead to electrochemical corrosion followed by the detachment of metal oxide from the support that results the rapid degradation of the electrode activity.[30] Therefore it will be desirable to use more robust non-carbon supports to avoid corrosion and prevent the agglomeration of metal oxides. To date ZnO has been demonstrated as an excellent mechanical support to improve the electrochemical performance of metal oxide electrodes.[22,30,32-37] However, the specific capacitance (152 F g^{-1} at 10 A g^{-1})[22] and electrochemical stability (~36% retention after 10 fold increment of current density) of these electrodes are poor at high current densities, which restrict severely its further use. In_2O_3 is one of the most attractive semiconductor materials and has a small specific capacitance, so it can function as efficient mechanical support and electron conducting channel. Prasad et al. reported the potentiodynamically deposited In_2O_3 nanostructure for redox capacitors showing a capacitance of 190 F g^{-1} at 10 mV s^{-1} with good capacity retention after 1,000 cycles.[38] In_2O_3/CNT(carbon nanotubes) heterogeneous films as an electrode for flexible and transparent supercapacitor showed a specific capacitance of 64 F g^{-1} with a cyclability of 500 cycles with 83% retention.[39] However, to the best of our knowledge there is no report on NiO-In_2O_3, which could bring a synergy between the advantages of both oxides. Thereby, in this work we designed and fabricated NiO-In_2O_3 heterostructured electrodes with a hierarchical 1D-3D hybrid nanostructure and study their synergistic contribution to pseudocapacitance. The design of this binder-free heterostructured electrode results in a high specific capacitance of 1096.8 F g^{-1} at 5 A g^{-1}, with an excellent rate performance (407.1 F g^{-1} at 30 A g^{-1}). The symmetric supercapacitor in a NiO-In_2O_3-NF /separator/ NiO-In_2O_3-NF configuration delivers an energy density of 21.1 Wh kg^{-1} at a power density of 1,500 W kg^{-1}, with excellent cycling stability. 79% of the initial capacitance is retained after 50,000 cycles, which is never been reported for oxide based material system. We believe this is due to rapid ion/electron transport, high conductivity, and the porous and integrated heterostructure of the NiO-In_2O_3 electrode material as opposed to their individual compounds.

Experimental Section

Material Synthesis: Growth of NiO-In_2O_3 hybrid structure on nickel foam: Nickel foam was cleaned ultrasonically in 3 M HCl, deionized (DI) water and ethanol for 15 min, respectively, and then dried in air. In a typical process, 0.1 mM $NiCl_2{\cdot}6H_2O$, 0.2 mM of $InCl_3$, 0.6 M of urea were dissolved into equal volume of DI water (40 ml) and ethanol (40 ml) mixed solvent to form a transparent green solution. After putting a piece of cleaned nickel foam (4 cm × 4 cm), the solution was then transferred to a reaction vessel and kept at 120 °C for 12 h. After hydrothermal growth, the nickel foam covered with NiIn-precursor was carefully rinsed several times with de-ionized water, absolute ethanol and acetone with the assistance of ultrasonication, and finally dried in air. Then, the sample was put in a muffle furnace and calcined at 400 °C for 2 h to get well defined crystallized NiO-In_2O_3 microflower/nanorod hybrid structure on nickel foam. For the sake of comparison, pure NiO, In_2O_3 and NiO-In_2O_3 hybrid composite with different concentration of Ni/In (1:1 and 2:1) also prepared using the same procedure. The mass of the hybrid structure on nickel foam was determined by subtracting the weight before deposition from the weight after deposition. Typical mass densities of active materials were about ~0.5 mg/cm^2, ~0.5 mg/cm^2, ~1.5 mg/cm^2, ~1.8 mg/cm^2 and ~1 mg/cm^2 for NiO-NF, In_2O_3-NF, NiO-In_2O_3-NF (1:1), NiO-In_2O_3-NF (1:2) and NiO-In_2O_3-NF (2:1) respectively. Figure S1 in Supplementary Information (SI) shows the photograph of NiO, NiO-In_2O_3 (1:2) and In_2O_3 grown on NF substrate.

Materials Characterization: The morphology and microstructure of NF-supported NiO-In_2O_3 electrodes were characterized using high resolution scanning electron microscope (FEI QUANTA 650 HRSEM), and high resolution transmission electron microscope (JEOL HRTEM-3010 at 200 kV). To avoid contribution of Ni from the NF, the EDX and XPS measurements were carried out for the powder samples scratched off from the NF. The crystal structure of the obtained samples was characterized by X-ray diffraction (XRD) (Philips X'Pert Pro; λ=0.1542 nm) with Cu Kα radiation. The Raman spectra of NiO-In_2O_3 hybrid structures were recorded with the Renishaw (RA 100) inVia confocal Raman Microscope at 514.5 nm excitation. The X-ray photoelectron spectroscopy (XPS) analysis was performed on a Perkin-Elmer PHI 550 spectrometer with Al K α (1486.6 eV) as the X-ray source.

Electrochemical Measurement: The electrochemical properties of the as-obtained hybrid electrodes were investigated using a three-electrode cell configuration at 25 °C. The nickel foam-supported NiO-In_2O_3 hybrid structure acted as the working electrode, which were soaked in a 3 M KOH solution and for 30 min before the electrochemical test. Platinum wire and a saturated calomel electrode (SCE) were used as the counter and reference electrodes, respectively. The electrochemical properties of symmetric supercapacitor were investigated in a two-electrode cell configuration with

NiO-In_2O_3-NF (1:2) hybrid electrode as the positive and negative electrodes in 3 M KOH electrolyte solution. The cyclic voltammetry (CV), galvanostatic charge-discharge, and electrochemical impedance spectroscopy (EIS) measurements were conducted using the CHI 660C (CH Instrument Company, USA) and Bio-Logic VMP3 electrochemical workstations.

Results and Discussion

Figure 1(a-d) shows SEM images of the structure and morphology of the nickel-indium oxide on nickel foam (NF). Low magnification SEM image of Figure 1(a) shows the formation of well integrated NiO-In_2O_3 hetero-microstructure over the nickel foam surface (inset of Fig. 1(a)). It contains uniformly grown flowers (Fig. 1(b and c)) comprised of ultra-thin nanosheets (Fig. 1(d)) with diameters ranging from 0.8-2 µm. Each nanosheet has a thickness in the range of 10-14 nm and has long planar dimensions.

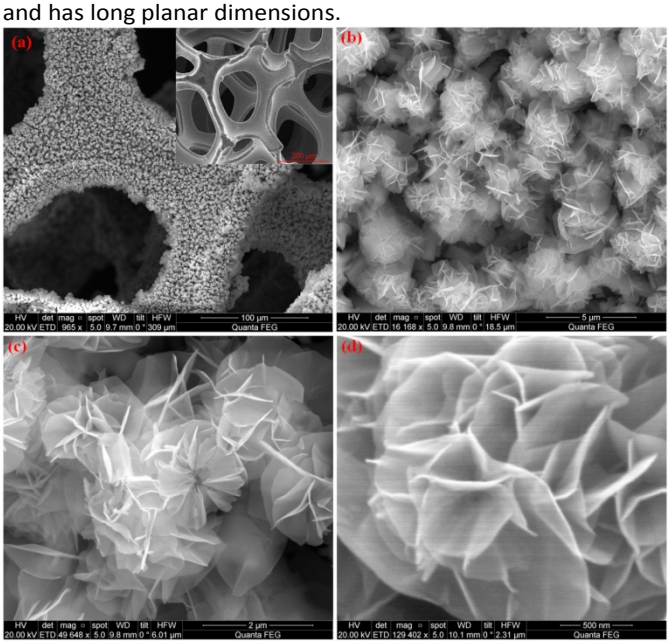

Fig. 1 (a-d) SEM images of NiO-In_2O_3-NF (1:2) hybrid structure at different magnifications.

Interestingly, all the flowers are supported by the nanorod arrays of several hundreds of nanometre in length with an average diameter of ~80 nm, as evidenced from the tilted angle SEM images in Fig. S2(a-d) of the Supplementary Information (SI).

To confirm the heterogeneous growth process, a time dependent synthesis was conducted using the same fabrication procedure with different timings of 3, 6 and 9 hours and the growth process is schematically represented in Figure 2. As evidenced from the time dependent experiments, In_2O_3 nucleates first as nanocubes and then grows as 1D nanorods. Simultaneously, NiO nucleated as 2D nanosheets and subsequently into a 3D microflower-like hierarchical architecture possibly due to crystal-face attraction, van der Waals force and hydrogen bonds.[4]

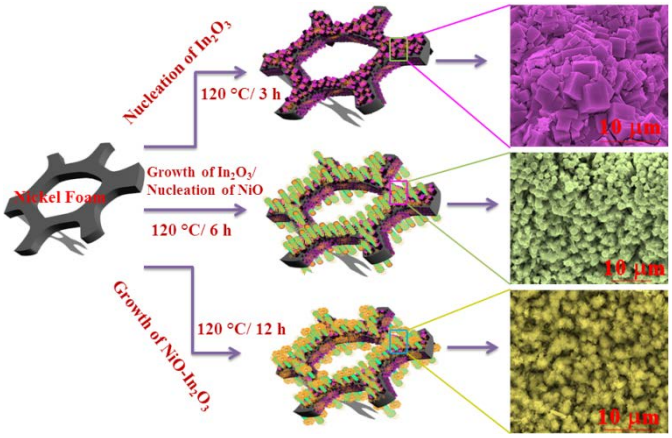

Fig. 2 Schematic description NiO-In_2O_3 hybrid structure growth process with the corresponding SEM images.

Finally, at the end of calcination, a well-defined and stable NiO-In_2O_3 hetero-microflower structure is formed as observed in the SEM images as shown in Figure S3(a-f). After 3 h, only nanorods covered with irregular microcubes mainly composed of In_2O_3 were present (Fig. S3(a and b)). At the end of 6 h, (Fig. S3(c and d)) a distinct microstructure of microcubes and nanoflowers are visible. Further increase of the growth time to 9 h, resulted in extensive growth of nano/micro flowers as seen in Fig. S3 (e and f). At the end of 12 h, typical 3D-1D hybrid microstructure was formed with the NiO-In_2O_3 hetero-composite. The growth process of this hybrid microstructure is discussed in detail in SI 2 of the supplementary section.

The energy dispersive X-ray spectroscopy (EDX) (Fig. S4(a-f) in Supplementary Information) of the NiO-In_2O_3 hetero-structures fabricated using 3 different mole concentrations of Ni:In (1:1, 1:2 and 2:1) confirms the presence of individual elements (Ni, In and O). However, hetero-structures showed variation in their elemental compositions, which may be attributed to the diffusion or formation of intermetallic compounds. Interestingly, for all the compositions, the regions over flowers (Figure S4(a, c & e)) show a dense distribution of Ni and a limited amount of In. On the other hand, the nanorod portion (Fig. S4 (b, d & f)) shows a dominant In distribution and low quantity of Ni. This observation further supports the formation of the hetero-composites. The deviation from initial concentration (Ni:In) suggests the partial incorporation of In and Ni ions within the NiO and In_2O_3 lattices during hydrothermal growth, which substantiates the formation of a solid solution. For better understanding of this microcube-nanorod-nano/microflower heterostructure formation, monometallic oxide of pure NiO and In_2O_3 were grown on the NF using similar fabrication method. Figure S5(a) and (b) are the SEM images and the corresponding EDX analysis of the NiO-NF (Fig. S5(e)) confirms the formation of highly dense networked nanosheets of NiO grown on the NF. By contrast, Figure S5(c) and (d) and the EDX of (f) reveal the irregular aggregates of In_2O_3 microcubes growth on the NF. The variations of elemental composition of both the pristine and mixed composites according to their Ni/In concentrations are tabulated in Table 1 of the supplementary information, which

further confirms the formation of NiO-In_2O_3 hetero-composites.

The elemental mapping of the sample scanned at different regions of nanorods, flowers and microflower/nanorod areas of the NiO-In_2O_3 (1:2) are displayed in Fig. 3(a), which shows the elemental distribution of Ni, In and O. Over the nanorod region, In is predominant with oxygen demonstrating the formation of In_2O_3. Alternatively, the flower area is extensively covered by the Ni with O, which reveals the growth of NiO microflowers over In_2O_3 nanorods. The dispersion of Ni and In in their respective nanorod and microflower regions indicates the partial diffusion/incorporation of metal ions in the hybrid composite lattices.

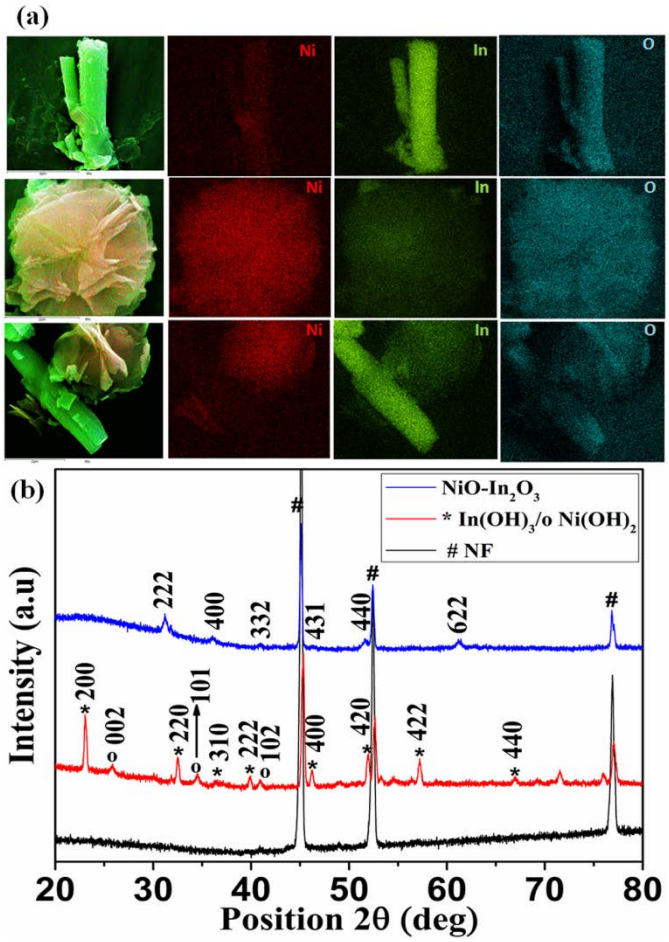

Fig. 3 (a) Elemental mapping spectrum of NiO-In_2O_3-NF (1:2) hybrid composite scanned at different regions, (b) XRD patterns of NiO-In_2O_3-NF (1:2) hybrid structure before and after calcination at 400 °C for 2 h.

To understand the crystal structure and phase of NiO-In_2O_3 hetero-structure, powder X-ray diffraction (XRD) was used. Figure 3(b) shows the XRD patterns of pure nickel foam and nickel indium oxide heterostructure (Ni:In/1:2) before and after calcination. In the mixed oxide, well-defined diffraction peaks are observed, which indicates the crystalline nature of the compound. Before the heat treatment at 400 °C, mixed hydroxide phases of $In(OH)_3$ and $Ni(OH)_2$ can be indexed to the corresponding JCPDS cards (#06-0202 and #22-0444).[40,41] Also some of the un-assigned peaks (≈49°, 53.3°, 54.5°, 56.3, 71.6° and 75.9°) can be visible in the mixed hydroxides due to intercalated charge balancing anions (i.e. CO_3^-, Cl^-) or water molecules.[43] After calcination, the hydroxides phases were completely converted to oxide phases, as evidenced from the corresponding EDX/elemental mapping analysis that correlates composition to structural morphology. When compared to pure monometallic oxides, the diffraction peaks in the XRD pattern of nickel indium oxide is well-matched to the cubic In_2O_3 phase (JCPDS # 06-0416)[42,43] as shown in Figure S7(a). To our surprise, there is no evidence of Ni based secondary phases in the NiO-In_2O_3 samples after calcination and it may be due to either the diffusion of Ni into the In_2O_3 lattice or insufficient/amorphous NiO phase formation, which is below the detection limit of the XRD (Figure S7(b)).[44]

To further investigate the nature of the NiO phase in the heterostructure, which could fall below the detection limit of XRD, Raman and high resolution TEM analysis were conducted. Typical Raman spectra shown in Fig. S8 indicates the formation of NiO-In_2O_3 hetero-composite. However the exact phase of Ni compound was still unclear. A brief discussion on Raman spectra according to the various concentrations of Ni/In are presented in the SI 3 of the supplementary section. Further inspection using high-resolution TEM (HRTEM) and the corresponding selected-area electron diffraction (SAED) shown in Fig. 4(a-f) reveal that these hybrid microflower/nanorods are polycrystalline in nature, as seen by the well-defined diffraction rings. TEM image in Fig. 4(a) clearly shows a distribution of fine nanocrystals of ~ 8-11 nm (inset Fig. 4(b)) in the nanorod region. Fig. 4(b) is the high magnification TEM image on nanorod portion showing the d-spacing of 0.29 nm for (222) planes of In_2O_3 oxide and 0.21 nm for (200) planes of NiO. The corresponding SAED pattern as shown in Figure 4(c) reflects the diffused rings of In_2O_3 and nearly amorphous NiO referring to the growth of nanocomposite.

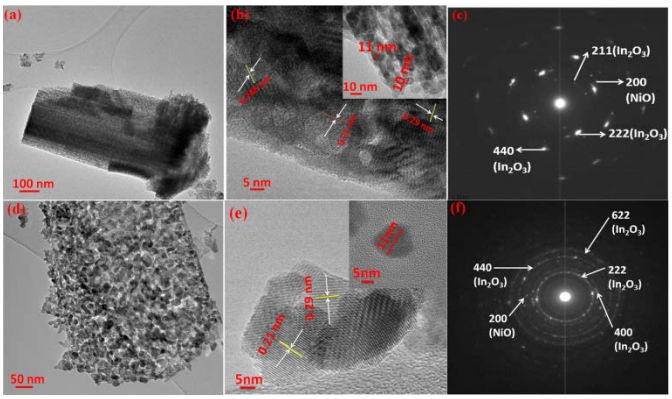

Fig. 4 HRTEM images of (a) NiO-In_2O_3 (1:2) hybrid structure, (b) nanorod region and (c) corresponding SAED pattern. (d) and (e) flower/ flakes region and (f) corresponding SAED pattern.

Figure 4(d) shows the petals of microflower structure comprised of fine nanocrystals with uniform particle distribution. These interconnected thin sheets (Fig. 4(e) and inset) self-assembled in such a way to form the final microflower structure where both 0.21 and 0.29 nm lattice

spacings are visible. A typical SAED image (Fig. 4(f)) shows the lattice spacing of 0.29, 0.18, 0.25, and 0.15 nm, in agreement with the (222), (440), (400) and (622) planes of In_2O_3, which is followed by the estimated lattice spacing of 0.21 nm for the (200) plane of NiO[26] and ultimately confirms the formation of nickel indium nanocomposite. All the rings in the SAED pattern in Fig. 4(f) can be indexed to the cubic In_2O_3 (# 06-0416) and NiO (# 47-1049). The samples were further analysed using XPS to investigate the formation NiO-In_2O_3 nanocomposite, and their appropriate valence states. Figure S9(a-c) represents the fine scan XPS spectra of pure NiO, In_2O_3 and different NiO-In_2O_3 composites. The de-convoluted XPS spectra of NiO-In_2O_3 composites obviously validate our perception of the hetero-structured composite which is composed of NiO-In_2O_3. A brief description of the XPS data and analysis is presented in SI 4 of the supplementary section which is in good agreement with the XRD and Raman analysis.

To demonstrate this NiO-In_2O_3 hetero-microflower as a supercapacitor electrode, a conventional three electrode cell was constructed and tested with electrochemical techniques such as cyclic voltammetry (CV), chronopotentiometry (CP) and electrochemical impedance spectroscopy (EIS).

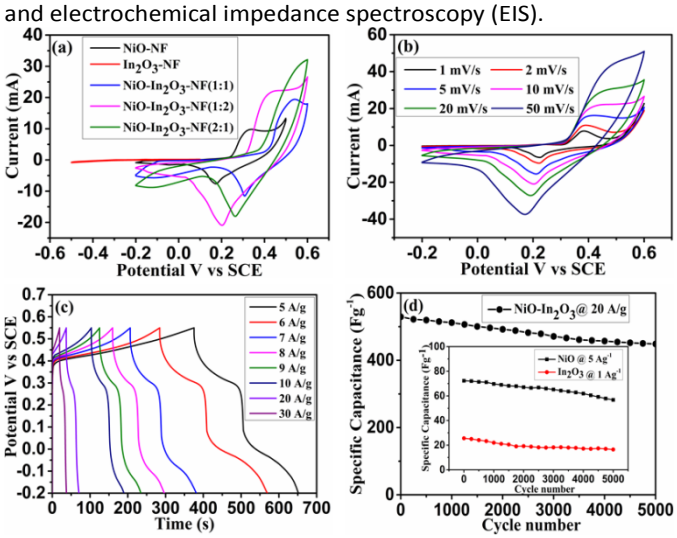

Fig. 5 (a) Cyclic voltammograms of individual oxides and NiO-In_2O_3-NF hybrid oxides measured at 10 mVs^{-1} in 3 M KOH. (b) Scan rate dependent cyclic voltammograms of NiO-In_2O_3-NF (1:2) hybrid electrode. (c) Charge-discharge profile of NiO-In_2O_3-NF (1:2) hybrid structure (d) Cyclic stability of NiO-In_2O_3-NF (1:2) at 20 A g^{-1} and the inset represents the cyclic stability curves of pristine oxides.

Typical CV curves of the NiO-NF, In_2O_3-NF and various compositions of NiO-In_2O_3-NF electrodes in 3 M KOH electrolyte at a scan rate of 10 mV s^{-1} are shown in Fig. 5(a), which show the pseudocapacitive characteristic of the electrodes. In order to understand the contribution of bare NF CV measurements of the NF before and after acid treatment was carried out at a scan rate of 10 mV s^{-1} and shown in Fig. S10. The estimated specific capacitance of the bare NF is 2.1 and 2.3 mF g^{-1} before and after the acid treatment. The comparison among the CVs in Fig. 5a indicates that the NiO-In_2O_3-NF (1:2) electrode possess a significantly higher specific capacitance than its individual oxides as well as the other Ni-In_2O_3 composites. This can be attributed to the synergistic contribution of both NiO and In_2O_3 to the specific capacitance associated to the hybrid microstructure. Figure 5(b) shows the CVs of the NiO-In_2O_3-NF(1:2) heterostructure over a range of scan rates of 1-50 mV s^{-1}. The pair of redox peaks between the potential limit of -0.2 to 0.6 V present in the CVs of mixed oxide indicate the dominant pseudocapacitive behavior,[45] which mainly originated from the faradaic reaction over the nickel oxide surfaces based on the following reaction (1);

$$NiO + OH^- \leftrightarrow NiOOH + H_2O + e^- \quad (1)$$

Figure 5(c) shows the charge-discharge profile of the NiO-In_2O_3-NF over a range of current density of 5-30 A g^{-1}. Symmetric features in the charge-discharge curves indicate good pseudo-electrochemical capacitance characteristic of the electrode, which stays symmetric even at a high current density of 30 A g^{-1}, indicating a high rate performance of the electrode. Noteworthy, the charge-discharge profile clearly evidences the contribution of In_2O_3 into redox process. It can be seen that the second redox process at 0 to -0.2 V is due to the redox reaction over In_2O_3 surface. So far, the investigation regarding In_2O_3 electrodes for supercapacitors is limited and therefore related reaction mechanism is not mentioned.[38,39,46] The exact redox mechanism is not clear and needs more investigations to understand the redox process. However, it is believed that in addition to redox process, In_2O_3 acts as an electron conducting channel between NF and NiO microflower. Furthermore, the partial incorporation of In^{3+} into NiO can increase the electrical conductivity of the NiO, which can increase the kinetics of NiO surface significantly in the hybrid electrode and will be discussed later by examining the EIS spectra of the electrodes. Also, the observed potential drop during discharge is higher than the acceptable value of ~1 mV. This can be explained by the ion depletion effect in the electrolyte, which increases the ionic resistance during redox processes.[47-49] The specific capacitance of the electrode was estimated using the relation (2):

$$C_s = I\Delta t / m\Delta V \quad (2)$$

where, I is the charge-discharge current, Δt is discharge time between the potential limit excluding IR drop, ΔV is the potential difference between cathodic and anodic peaks, and m is the weight of the active material. Figure S11 shows the variation in specific capacitance with the current density ranging from 5-30 A g^{-1} in 3 M KOH solution in three electrode configuration. The specific capacitance of this hybrid composite electrode varies from 1096.9 to 407 F g^{-1} for a current density ranging from 5 to 30 A g^{-1}. Thereby, the electrode can retain 37.1% of its initial value for 6 times of initial current density. The observed specific capacitance value for our NiO-In_2O_3-NF are far better than the similar hetero-composite oxide and chalcogenides based electrode materials as shown in Table 2 of the supplementary information. Pu *et al*. achieved ultra-high specific capacitance of 2028 F g^{-1} at 10 A g^{-1} with $Ni(OH)_2$@ZnO, but the cyclic stability was limited to 68% after 500 cycles.[34] Similarly, Xing *et al.* reported 1529 F g^{-1} at 2 A g^{-1} with 42% capacity retention after 2,000 cycles in Ni_3S_2@ZnO hetero-structure.[36] Furthermore, Wang *et al.* showed 1716 F g^{-1} at 1 A g^{-1} in the $NiCo_2O_4$@Ni_3S_2 core/shell nanothorn arrays electrode with 83.7% capacity retention.[50]

When compared to these electrodes our NiO-In_2O_3 electrode exhibit acceptable specific capacitance (1096.8 F g^{-1} at 5 A g^{-1}) but delivers excellent capacity retention of 89.5% after 5000 cycles. Also, these values are much higher than the electrodes made from individual compounds as we can see from the charge-discharge curves in Fig. S12(a and b), with measured specific capacitances of 450 F g^{-1} (@ 1 A g^{-1}) and 49 F g^{-1} (@ 0.7 A g^{-1}) for NiO-NF and In_2O_3-NF respectively. The low specific capacitance for NiO and In_2O_3 can be attributed to their unfavourable microstructure for ion diffusion and low intrinsic electrical conductivity. The electrical conductivity was further investigated by EIS analysis and presented in Fig. S13. From the extended view of Nyquist plot in Fig. S13 inset, it can be seen that the NiO-In_2O_3-NF hybrid electrode showed negligible charge transfer resistance of ~ 0.08 Ω, which indicates the incorporation of In^{3+} ion have increased the electrical conductivity of hybrid electrode significantly. Whereas, pure NiO-NF electrode showed visible semicircle at high frequency region followed by sloped straight line resulted in a charge transfer resistance of 0.45 Ω.[12,50,51] However, the pristine In_2O_3-NF have shown a distinct EIS spectra. Due to limited measurement frequency, there is incomplete depressed semicircle at high frequency region, visible semicircle at middle frequency range and a sloped line in the low frequency region.[52,53] Here in the Nyquist plot, the high-frequency intercept on the real axis is mainly composed of the bulk resistance of electrode materials, resistance of the current collector and contact resistance.[52] Meantime, intercept at high-mid frequency represents the charge transfer resistance of the electrode materials. The sloping line in the low-frequency range ascribes the proton diffusion into the bulk electrodes, known as the Warburg impedance.[12] From EIS results, it can be confirmed that the hybrid electrode possess better electrical conductivity than the pristine materials and thereby enhanced electrochemical performance have been observed.

Similarly, the electrochemical performance of other compositions namely, NiO-In_2O_3 (1:1) and (2:1) were also evaluated and the results are discussed in SI 5 of the supplementary section. Interestingly, among the three compositions, NiO-In_2O_3-NF (1:2) showed the best electrochemical performance in terms of specific capacitance and rate capability, which is mainly attributed to their well-integrated 3D-1D hybrid microstructure. When compared to the monometallic oxides, the mixed NiO-In_2O_3-NF (1:2) electrode has delivered two orders of magnitude increased specific capacitance (when compared to In_2O_3-NF) and three order superior rate performance. Interestingly, the observed specific capacitance is even higher than the synergistic limit of individual oxides further revealing the extra-ordinary performance of the hetero-structured electrode, driven by the three dimensional hierarchical microstructure. We demonstrated that the nanorods-supported microflower heterostructure provides improved electron transfer kinetics and thus significantly increased specific capacitance. One dimensional nanorods not only served as a scaffold for electrochemically active materials, but also served as effective channels for electron transfer between the active nano/microflower and the NF substrate.[35] Another important requirement for supercapacitor applications is its long term cyclic stability. Hence, the charge-discharge cycle was repeated up to 5,000 cycles at 20 A g^{-1} as depicted in Figure 5(d). When compared to individual oxides, the hybrid electrode shows only 10.5% capacitance loss after 5,000 cycles, while it was 21.5% and 35.6% for NiO-NF and In_2O_3-NF (Inset of Figure 5(d)). Due to the unique structural and conductive support, the NiO-In_2O_3-NF (1:2) is expected to retain excellent electrochemical properties as supercapacitor electrodes.

For practical application, sandwich type symmetric supercapacitor device was fabricated using two pieces of NiO-In_2O_3-NF electrodes separated by Celgard separator and tested in 3 M KOH aqueous electrolyte. Fig. 6(a) shows the CV curves of the symmetric supercapacitor device at scan rates extending from 5 to 50 mV s^{-1}. Distinct CV curves indicate the capacitive characteristic of the device as a function of scan rate. Further increasing the scan rate from 75 to 500 mV s^{-1} did not result any obvious changes (Fig. S15), implying the high rate capability of the device.

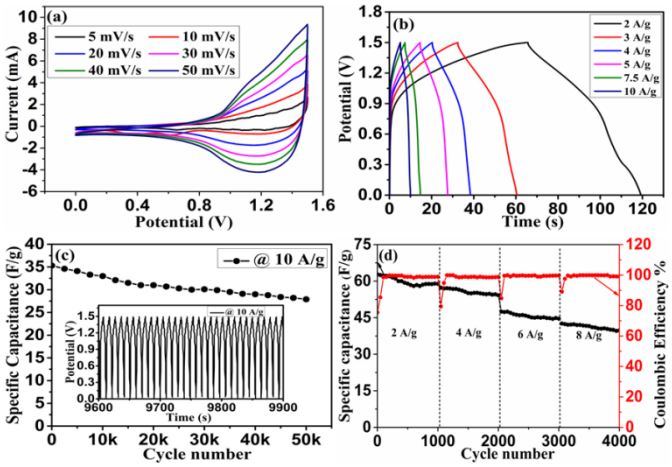

Fig. 6 (a) Cyclic voltammograms of symmetric supercapacitor fabricated with NiO-In_2O_3-NF (1:2) hybrid structure at different scan rates in 3 M KOH. (b) Charge-discharge curves of NiO-In_2O_3-NF (1:2) based symmetric supercapacitor at various current densities. (c) Cyclic stability of the symmetric supercapacitor and inset represents continuous charge-discharge profile at 10 A g^{-1} (d) Capacity retention and coulombic efficiency of the device at different current density.

Figure 6(b) shows the galvanostatic charge-discharge curves of the symmetric supercapacitor, which is carried out at different current densities (2-10 A g^{-1}). Nearly symmetric charge-discharge behaviour envisages the capacitive features. The specific capacitance of the device is evaluated using equation (2), where the total mass of the device is ~1 g inclusive of two electrodes and the separator. The estimated specific capacitance for the symmetric supercapacitor is found to be 67.6 F g^{-1} at a constant current density of 2 A g^{-1}. When the current density is increased, the capacitance decreases due to the fact that insufficient active materials involve in the redox reaction. However, our device still exhibits 35.3 F g^{-1} of specific capacitance even at a high current density of 10 A g^{-1}, which is

52% of the initial capacitance when the current density is increased by a factor of 5. With increasing current density, the specific capacitance varies significantly as shown in Figure S9. The observed Cs value is much higher than the earlier reported values of 22 F g^{-1} for Ni|KOH|Ni symmetric supercapacitor,[54] 44 F g^{-1} for Co(OH)2/SS(stainless steel) electrodes[55] and quite comparable to the Co(OH)2/GF (graphene foam) electrode of 69 F g^{-1} [56] in symmetric supercapacitor configurations. Furthermore, the supercapacitor shows outstanding cyclic stability (Figure 6(c)), with only 21% capacitance loss after 50,000 cycles. The excellent cyclic stability may be attributed to a well-integrated and strongly adhered NiO-In_2O_3 hierarchical nano/micro architecture on the nickel foam substrate and their synergistic effect. In terms of coulombic efficiency, our device has showed significant variations based on the applied current density. Fig. 6(d) shows the variation of specific capacitance and the corresponding coulombic efficiency measured at various current densities of 2 – 8 A g-1. Worth mentioning, the estimated capacity retentions were about ~94% for all current densities after 1000 cycles. However, the coulombic efficiency varied significantly during initial few cycles. Fig. S16(a-d) shows the initial charge/discharge cycles of fabricated symmetric supercapacitor measured at before and after 1000 cycling. From Fig. S16, the calculated efficiency values for first 5 cycles are 75.5%, 79.4%, 84.76% and 89.1% for the current density of 2, 4, 6 and 8 A g-1, respectively. It reaches to ~98% of the maximum value after prolonged cycling as shown in Fig. S17 (a-d). This can be explained by the effect of solid electrolyte interphase (SEI) layer formation over electrode materials during redox reaction. It is well demonstrated that the generation of SEI layer plays a crucial role in batteries and hybrid supercapacitors.[57-60] Generally, the SEI layer is created on an electrode surface due to the reaction between solid electrode and liquid electrolyte.[57] In our case, it is believed that typical SEI layer is formed on the electrode surface during initial charge/ discharge cycles as reported earlier.[57,59,60] The detailed mechanism of SEI layer formation is not clear and needs further investigations. The same trend in efficiency was observed for all the measured current densities as shown Fig. 6(d), which indicates that the formation of SEI layer is independent to the applied current density. However, the SEI formation requires only few 10s of cycles at high current density, whereas it is nearly 100 cycles for low current density. The variation in efficiency can be directly related to the electrode kinetics during redox process. Since the NiO and In_2O_3 have different kinetic potentials, the redox process is also different during charging/ discharging process, thereby asymmetric behaviour is observed in Fig. 5(c) and Fig. 6(b). Also, the formation of stable SEI layer ensures the long term cyclic stability of the device.[58]

The energy and power densities are two important factors to evaluate the performance of a supercapacitor, which were calculated using the following equations:

$$E = CV^2/2 \quad (3)$$

$$P = (E/t) \quad (4)$$

Here, E is the energy density (Wh kg^{-1}), P is the power density (W kg^{-1}), C is the specific capacitance (F g^{-1}), V is the potential (V) and t is discharge time (s).

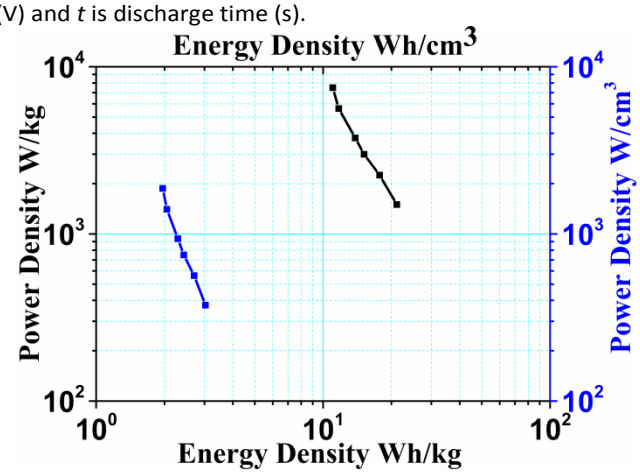

Fig. 7 Ragone plot for NiO-In_2O_3-NF (1:2) based symmetric supercapacitor.

According to the Ragone plot shown in Figure 7, the highest energy density for our supercapacitor is 21.1 Wh kg^{-1} with a power density of 1500 W kg^{-1} and remained 11.3 Wh kg^{-1} at a maximum power density of 7492.9 W kg^{-1}. The corresponding volumetric energy and power density for our symmetric supercapacitor is about 5.27 Wh cm^{-3} and 374.5 W cm^{-3}. The observed energy and power performance for the NiO-In_2O_3 hybrid structure is higher than most of the reported symmetric supercapacitors.[54-56] In order to demonstrate practical usability of the device, three symmetric cells were connected in series and lighting a red LED for 10 seconds while discharging (Fig. S18 (a)). Furthermore, the device which fabricated with NiO-In_2O_3 was lighting an LED with the same power (Fig. S18 (b)) even a month after the initial test. Thus further confirms the long-term activity of the electrode for high performance supercapacitor applications. The electrochemical impedance spectroscopy was performed to study the resistance of the supercapacitor device before and after 50,000 cycles (Fig. S19). Both plots consists of semicircle arcs at high to middle frequency region and straight lines at low frequency range. The observed EIS data can be fitted with the equivalent circuit (inset of Figure S19) consisting of solution resistance (R_s), charge transfer resistance (R_{ct}), diffusion resistance (W) and electrochemical capacitance (C_{dl}).[51] The Nyquist plot revealed no obvious resistance change of the device even after 50,000 cycles, which is remarkable. However, the deviation in the slope of the straight line confirms the increased internal resistance at the electrode. Thereby, the EIS results further confirm the excellent stability of the symmetric capacitor.

The superior electrochemical performance of the NiO-In_2O_3 heterostructured electrode could be attributed to the following structural benefits: First, 3D mesoporous NF has superior electrical conductivity and this leads to rapid electron transport during charge-discharge process at high current density. Second, the 3D-1D hybrid micro-/nano structure gives more active sites for redox reactions due to the existence of more surface defects on the oxide surface as observed in the

XPS analysis and their synergistic contribution. Third, 1D nanorod integrated hierarchical microflower structure increases the cyclic stability for long term applications due to strong mechanical integrity with Ni support. Moreover, these 1D nanorods not only support the electroactive materials, but also serve as effective channels for electron transfer and act as an intermediate buffer layer between the highly active NiO flower and the Ni foam substrate. Finally, formation of strongly coupled NiO-In_2O_3 heterostructures with mesoporous Ni foam resulted in a large contact area between active materials and the electrolyte, leading to more efficient ion and charge transport, resulting in significant increases in the specific capacitance and rate capability at high current densities over longer cycle times.

Conclusions

In summary, we have designed and synthesized hierarchical 3D/1D hybrid NiO-In_2O_3 hetero-structures via facile hydrothermal technique on three dimensional nickel foam substrates. This interesting hetero-architecture allows the synergistic contribution of both nanostructure as well as materials leading to better electrochemical performance as a supercapacitor electrode. Noticeably, by varying the compositions these hetero-structured electrodes showed distinct electrochemical performances due to their diverse electron/ion transfer kinetics and microstructure. Among them, the hierarchical hybrid structures of NiO-In_2O_3 (1:2) electrode delivered a high specific capacitance of 1096.8 F g^{-1} at 5 A g^{-1} in 3 M KOH electrolyte. Here, the 1D nanorod structure not only served as the conducting scaffold for 3D microflower but also acted as channel for the efficient electron/ion transport. Due to the well-integrated microflower/nanorod structure with NF support, the symmetric supercapacitor fabricated using this electrode (NiO-In_2O_3 (1:2)) showed a high specific energy density of 21.1 Wh kg^{-1} with the specific power density of 1500 W kg^{-1}. This hetero-electrode made supercapacitor further showed largely enhanced cyclic stability with only 21% loss after 50,000 cycles. Therefore, it can be suggested that the design and one pot synthesis of this novel 3D-1D hierarchical hetero-nanostructure could be an effective way to enhance the pseudocapacitance of the electrode materials.

Acknowledgements

The authors acknowledges the financial support from EU FP7 project MANpower (contract number: 604360) to carry out this work. We acknowledge support from Science Foundation Ireland under a Technology Innovation and Development Award no. 14/TIDA/2455 and 13/TIDA/E2761. This research has received funding from the Seventh Framework Programme FP7/2007-2013 (Project STABLE) under grant agreement no. 314508.

Notes and references

1 P. Simon, Y. Gogotsi, *Nat. Mater.,* 2008, **7**, 845.
2 A. S. Arico, P. Bruce, B. Scrosati, J. M. Tarascon, W.Van Schalkwijk, *Nat. Mater.,*2005, **4**, 366.
3 M. Winter, R. J. Brodd, *Chem. Rev.,* 2004, **104**, 4245.
4 P. Simon, Y. Gogotsi, *Accounts of Chemical Research,* 2011, **46**, 1094.
5 J. R. Miller, P. Simon, *Science,* 2008, **321**, 651.
6 Y. Xiao, S. Liu, F. Li, A. Zhang, J. Zhao, S. Fang, D. Jia, *Adv. Funct. Mater.,* 2012, **22**, 4052.
7 M. Inagaki, H. Konno, O. Tanaike, *J. Power Sources,* 2010, **195**, 7880.
8 W. Sugimoto, H. Iwata, Y. Yasunaga, Y. Murakami, Y. Takasu, *Angew. Chem. Int. Ed.,* 2003, **42**, 4092.
9 W. Wei, X. Cui, W. Chen, D. G. Ivey, *Chem. Soc. Rev.,* 2011, **40**, 1697.
10 Z. Lu, Z. Chang, J. Liu, X. Sun, *Nano Res.,* 2011, **4**(7), 658.
11 G. Wang, L. Zhang, J. Zhang, *Chem. Soc. Rev.,* 2012, **41**, 797.
12 J. Li, F. Luo, Q. Zhao, Z. Li, H. Yuan, D. Xiao, *J. Mater. Chem. A*, 2014, **2**, 4690.
13 X. Tian, C. Cheng, L. Qian, B. Zheng, H. Yuan, S. Xie, D. Xiao, M. M. F. Choi, *J. Mater. Chem.*, 2012, **22**, 8029.
14 N. Padmanathan, S. Selladurai, K. M. Razeeb, *RSC Adv.,* 2015, **5**, 12700.
15 L. Huang, D. Chen, Y. Ding, S. Feng, Z. L. Wang, M. Liu, *Nano Lett.,* 2013, **13**, 3135.
16 K. M. Hercule, Q. Wei, A. M. Khan, Y. Zhao, X. Tian, L. Mai, *Nano Lett.,* 2013, **13**, 5685.
17 L. Xu, Y. Su, S. Li, Y. Chen, Q. Zhou, S. Yin, Y. Feng, *J. Phys. Chem. B*., 2007, **111**, 760.
18 J. Xiao, J. Zheng, X. Li, Y. Shao, J. G. Zhang, *Nanotechnology,* 2013, **24**, 424004.
19 Y. Li, Z. Y. Fu, B. L. Su, *Adv. Funct. Mater.,* 2012, **22**, 4634.
20 C. Liu, F. Li, L. P. Ma, H. M. Cheng, *Adv. Mater.,* 2010, **22**, E28.
21 W. Tian, X. Wang, C. Zhi, T. Zhai, D. Liu, C. Zhang, D. Golberg, Y. Bando, *Nano Energy,* 2013, **2**, 754.
22 M. Huang, F. Li, X. L. Zhao, D. Luo, X. Q. You, Y. X. Zhang, G. Li, *Electrochim. Acta,* 2015, **152**, 172.
23 A. Ramadoss, S. J. Kim, *Electrochim. Acta,* 2014, **136**, 105.
24 S. Vijayakumar, S. Nagamuthu, G. Muralidharan, *ACS Appl. Mater. Interfaces,* 2013, **5**, 2188.
25 A. K. Singh, D. Sarkar, G. G. Khan, K. Mandal, *ACS Appl. Mater. Interfaces,* 2014, 6, 4684.
26 C. Y Cao, W. Guo, Z. M. Cui, W. G. Song, W. Cai, *J. Mater. Chem.,* 2011, 21, 3204.
27 M. Huang, F. Li, J. Y. Ji, Y. X. Zhang, X. L. Zhao, X. Gao, *Cryst. Eng. Comm.,* 2014, 16, 2878.
28 L. Shen, Q. Che, H. Li, X. Zhang, *Adv. Funct. Mater.,* 2014, **24**, 2630.
29 X. Wu, L. Jiang, C. Long, T. Wei, Z. Fan, *Adv. Funct. Mater.,* 2015, **25**, 1648.
30 Y. B. He, G. R. Li, Z. L. Wang, C. Y. Su, Y. X. Tong, *Energy Environ. Sci.,* 2011, **4**, 1288.
31 D. Kong, J. Luo, Y. Wang, W. Ren, T. Yu, Y. Luo, Y. Yang, C. Cheng, *Adv. Funct. Mater.,* 2014, **24**, 3815.
32 G. R. Li, Z. L. Wang, F. L. Zheng, Y. N. Ou, Y. X. Tong, *J. Mater. Chem.,* 2011, **21**, 4217.
33 D. Cai, H. Huang, D. Wang, B. Liu, L. Wang, Y. Liu, Q. Li, T. Wang, *ACS Appl. Mater. Interfaces,* 2014, **6**, 15905.
34 Z. Pu, Q. Liu, A. H. Qusti, A. M. Asiri, A. O. Al-Youbi, X. Sun, *Electrochim. Acta,* 2013, **109**, 252.
35 M. Huang, F. Li, X. L. Zhao, D. Luo, X. Q. You, Y. X. Zhang, G. Li, *Electrochim. Acta,* 2015, **152**, 172.
36 Z. Xing, Q. Chu, X. Ren, C. Ge, A. H. Qusti, A. M. Asiri, A. O. Al-Youbi, X. Sun, *J. Power Sources,* 2014, **245**, 463.
37 X. Sun, Q. Li, Y. Lu, Y. Mao, *Chem. Commun.,* 2013, **49**, 4456.
38 K. R. Prasad, K. Koga, N. Miura, *Chem. Mater.,* 2004, **16**, 1845.

39 P. C. Chen, G. Shen, S. Sukcharoenchoke, C. Zhou, *Applied Physics Letters,* 2009, **94**, 043113.
40 Y. Ren, L. Gao, *J. Am. Ceram. Soc.,* 2010, **93**, 3560.
41 D. Chu, Y. Masuda, T. Ohji, K. Kato, *Langmuir,* 2010, **26**, 14814.
42 C. Wang, D. Chen, X. Jiao, C. Chen, J. Phys. Chem. C, 2007, **111**, 13398.
43 J. Liu, T. Luo, F. Meng, K. Qian, Y. Wan, J. Liu, J. Phys. Chem. C, 2010, **114**, 4887.
44 H. J. Kim, H. M. Jeong, T. H. Kim, J. H. Chung, Y. C. Kang, J. H. Lee, ACS Appl. Mater. Interfaces, 2014, **6**, 18197.
45 L.Yang, S. Cheng, Y. Ding, X. Zhu, Z. L. Wang, M. Liu, Nano Lett., 2012, **12**, 321.
46 J. Chang, W. Lee, R. S. Mane, B. W. Cho, S.H. Han, Electrochem. Solid-State Lett, 2008, **11**(1) A9.
47 I.H Kim, J. H. Kim,K. B. Kim, Electrochem. Solid-State Lett, 2005, **8**(7) A369.
48 J.P. Zheng, P.J. Cygan, and T. R. Jow, *J. Electrochem. Soc.*, 1995, **42**, 2699.
49 N. Nagarajan, I. Zhitomirsky, *J. Appl. Electrochem.*, 2006, **36**, 1399.
50 J. Wang, S. Wang, Z. Huang, Y. Yu, *J. Mater. Chem. A*, 2014, **2**, 17595.
51 S. Li, J. Wen, X. Mo, H. Long, H. Wang, J. Wang, G. Fang, J. Power Sources, 2014, 256, 206.
52 B. Zhang, Y. H. Li, J. H. Zhong, X. H. Yang, H. M. Zhang, H. J. Zhao, H. G. Yang, *J. Mater. Chem. A*, 2014, **2**, 6331.
53 L. Yue, W. H. Zhang, W. Zhang, Q. Zhang, R. Guan, G. Hou, N. Xu, *Electrochim. Acta*, 2015, **160**, 123.
54 V. Ganesh, S. Pitchumani, V. Lakshminarayanan, J. Power Sources, 2006, **158**, 1523.
55 A.D. Jagadale, V.S. Kumbhar, D.S. Dhawale, C.D. Lokhande, Electrochimica Acta, 2013, **98**, 32.
56 U.M. Patil, S. C. Lee, J. S. Sohn, S. B. Kulkarni, K. V. Gurav, J. H. Kim, J. H. Kim, S. Lee, S. C. Jun, Electrochimica Acta, 2014, **129**, 334.
57 M.G. Choi, S. B. Kang, J. R. Yoon, B. G. Lee, D.Y. Jeong, J Electr. Eng. Technol., 2015, **10**, 30.
58 G. Gourdin, D. Zheng, P. H. Smith, D. Qu, Electrochim. Acta, 2013, **112**, 735.
59 Y. Wang, X. Guo, S. Greenbaum, J. Liu, K. Amine, Electrochem. Solid-State Lett., 2001, **4**(6), A68.
60 J. H. Lee, W. H. Shin, S. Y. Lim, B. G. Kim, J. W. Choi, Mater. Renew. Sustain. Energy, 2014, **3**, 22.